Advances in Functional Materials (Conference 2015), AFM 2015

Hybrid Modeling of Molecular Sensing and Catalysis in Low-dimensional Nanomaterials

Artem Baskin[a,b] and Petr Král[b,c]*

[a]*Lawrence Berkely National Laboratory, Molecular Foundary, 1 Cyclotron Rd., MS 67-3207 Berkeley, CA 94720, USA*
[b]*University of Illinois at Chicago, Department of Chemistry, 845 W. Taylor St., Chicago, IL 60607, USA*
[c]*University of Illinois at Chicago, Department of Physics, 845 W. Taylor St., Chicago, IL 60607, USA*

Abstract

We use hybrid quantum and classical modeling to describe recently observed molecular sensing at graphene grain boundaries and electrochemical reduction of carbon dioxide (CO_2) on molybdenum disulphide (MoS_2) flakes. In the sensing studies, classical and quantum molecular dynamics simulations are used to relax graphene with grain boundaries deposited on amorphous SiO_2. Electronic structure calculations show how this graphene is locally doped by the substrate and adsorbed molecules, while electronic transport modelling reveals that the doping can lead to synchronous opening and closing of local electron transport channels, resulting in a very large observed sensitivity. In the catalysis studies, electronic structure calculations combined with *ab initio* molecular dynamics uncover that the metallic character and high d-electron density of molybdenum-terminated MoS_2 edges and EMIM-ion delivery are responsible for the observed superior CO_2 reduction performance, with a high current density and low ~54 mV overpotential. The described mechanisms open up new pathways for the design of nanometer-scale highly sensitive chemical detectors and the development of inexpensive systems of CO_2 conversion to energy-rich products. These studies illustrate how hybrid modeling techniques can explain complex transport phenomena in nanostructures.

* Corresponding author. Tel.: +1 312-996-6318; fax: +1 312-996-0431.
E-mail address: pkral@uic.edu

1. Introduction

Over the last two decades, ground breaking innovations led to the preparation and characterization of many unique nanoscale materials. However, reproducible preparation of nanoscale material with tunable properties necessitates detail understanding of the microscopic mechanisms responsible for their behavior. Realistic modeling of such material systems requires a coherent combination of many different computational approaches. In this work, we illustrate the use of such hybrid modeling on a molecular sensing at graphene grain boundaries (GB) and an electrochemical CO_2 reduction on MoS_2 flakes.

Due to its single atom thickness and peculiar electronic properties [1,2], graphene was anticipated to be an ideal platform for molecular sensing. However, it turned out that a nearly electron-hole symmetrical structure with vanishing concentration of carriers at the Dirac point preclude successful use of pristine graphene for molecular sensing. Molecular sensing in functionalized and geometrically modified graphene-based nanostructures, including nanopores and heterojunctions, was also tested [3,4,5]. For example, zero-dimensional topological defects, with an efficient physisorption of gas molecules, were considered to improve the sensitivity of such sensors [6-12]. However, these defects only moderately improved chemical and molecular sensing of graphene sensors [13]. Recently, graphene GBs were shown to serve as highly sensitive and selective molecular sensors [14]. Here, we show how in detail how hybrid simulations can explain these complex phenomena.

Heterogeneous catalysis also largely benefited from the reduced dimensionality of potential catalysts. MoS_2 became widely used as an efficient catalyst for hydrodesulphurization [15,16], oxygen reduction reactions [17] and hydrogen evolution reaction (HER) [16,17]. Moreover, MoS_2 was demonstrated to have a noteworthy performance for water splitting, approaching that of Pt-group metals [17,18,19]. However, the development of systems with an efficient carbon dioxide reduction capability remains a challenge [20-24]. The CO_2 reduction by electrochemical processes faces fundamental and practical challenges caused mainly by a high cost and unsatisfactory conversion performance of existing catalytic systems [20]. Numerous physical and chemical approaches have been shown to improve the performance of existing CO_2 reduction systems [25-29]. Recently, it was reported that the layer-stacked bulk MoS_2 with molybdenum (Mo)-terminated edges exhibits one of the highest observed CO_2 reduction performance [30]. Here, we again detail our hybrid simulations revealing the origins of such high catalytic activity.
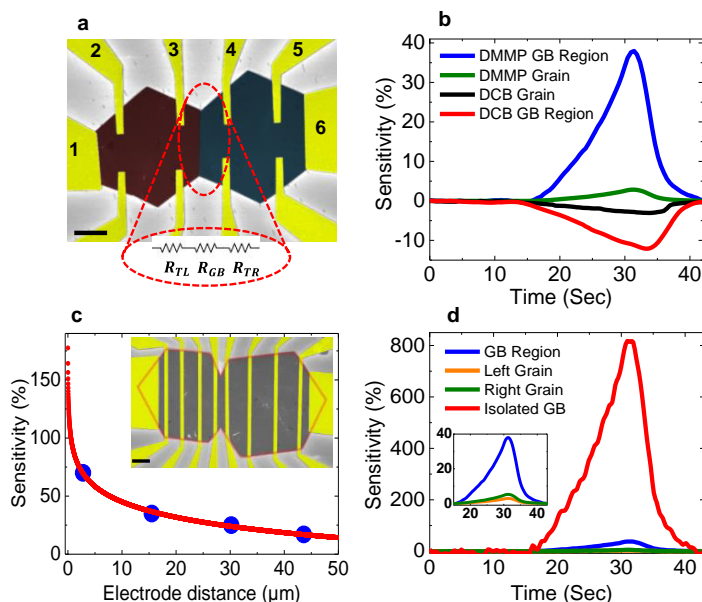

Fig. 1. Sensing properties of an individual graphene grain boundary (GB). (a) False-colour SEM image of a typical fabricated GB-sensing platform (scale bar, 5 mm). A corresponding electrical circuit is also shown. (b) Sensing signal for the dimethyl methylphosphonate (DMMP) and 1,2-dichlorobenzene (DCB) gas molecules. (c) Fabricated multi-electrodes single-GB-sensing platform (scale bar, 5 mm) and the

sensitivity of the GB devices with respect to the distance from the electrodes. (d) Sensitivity of the isolated GB against DMMP molecules extracted from the real-time sensing measurements. The inset magnifies the same curves. [14]

2. Chemical sensing on graphene grain boundaries

2.1 *Experimental results*

We start by briefly describing the observed superior molecular sensing at graphene GBs [14]. Figure 1a shows a scanning electron microscopy (SEM) image of an individual GB chemical-sensing platform. Its sensing characteristics was studied by monitoring the resistance change (current flow across GB) upon exposure to gas molecules and comparing it with this change observed in the individual gas-exposed graphene grains. In the sensing experiments, a known concentration (50 p.p.b.) of gas molecules (dimethylmethylphosphonate (DMMP) and 1,2-dichlorobenzene (DCB)) were injected over the sensing platform in ambient conditions. DMMP and DCB analytes were selected due to their electron-donating and electron-accepting nature, respectively. Figure 1b shows a typical sensing response towards DMMP and DCB molecules for grains and the GB region. The sensitivity is defined as $S=(R-R_0)/R_0$, where R_0 and R are the initial and final resistance (after gas exposure), respectively. Upon injection of the selected gas molecules, positive and negative change of resistance was obtained in the electron-donating and electron-accepting molecules, respectively [31]. For DMMP, the sensitivity of GB sensors (39.5%) is ~1 order of magnitude (14 times) higher than that of the grain sensors (2.8%). For DCB, the sensitivity of GB sensors (11%) is almost five times higher than that of the grain sensors (2.3%). Upon isolation of an individual GB, even higher sensitivity was recorded. Figure 2d shows the time-dependent sensitivity of the isolated GB upon exposure to pulse of gas, which is at the maximum ~ 300 times higher than that of the adjacent single-crystalline grains under identical experimental conditions.

2.2 *Simulation of molecular sensing*

In order to clarify these striking observations, we need to describe: (1) the atomistic and electronic structure of the GB system deposited on an amorphous SiO_2 substrate and in adsorbed analytes molecules and (2) the electronic transport through the stabilized GB system.

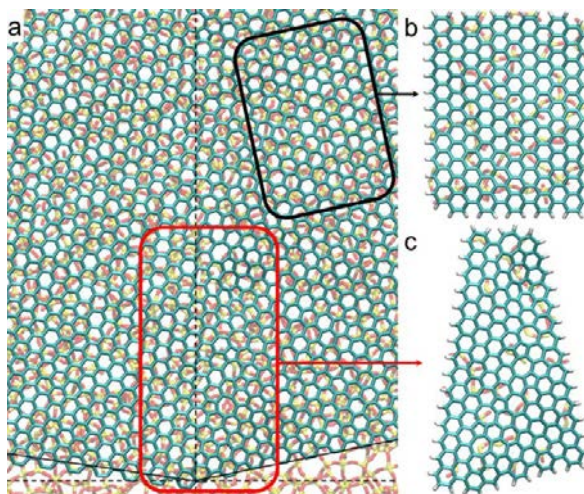Fig. 2 Hybrid MD simulations. (a) Graphene with the GB between two grains with a mismatch angle of 18º. (b-c) Representative regions: pristine and defective, respectively.

To address the **first task**, we first prepare a system containing two pristine graphene grains (Fig. 2 a) with a mismatch angle of 18º giving a GB between them. The model defective meandered GB includes two local regions, which are characterized by their crystallographic orientations of grains, local angles of GB with respect to the grains, and local topologies of GB defects compatible with a mismatch angle of 18º. We relax the neutral system (pristine

grains + GB + SiO$_2$ substrate) by classical molecular dynamics (MD) simulations (t~5 ns), using NAMD [32,33] and the CHARMM32 force field [34], gradually improved in quantum MD simulations. To evaluate the doping (charge transferred) from an amorphous SiO$_2$ substrate, we extract from the whole system two representative parts (Fig. 2) containing the pristine grains and GBs on SiO$_2$ with dangling bonds (Fig. 2 b-c), where the graphene edges are passivated by H atoms. We calculate the atomic charges of the combined structures by *ab initio* molecular dynamics (AIMD) simulations with TeraChem [35-37]. We found that a charge of 0.265e is transferred from the graphene system to the substrate (p-doping), which is comparable to 0.362e reported for analogous systems [38,39]. Using these atomic charges, we estimate in classical MD simulations the adsorption of DMMP molecules on pristine and defective regions. To account for the effect of the charge transfer from the electron donor DMMP molecules to the GB, we also perform AIMD simulations (t~1 ps) of the GB on the SiO$_2$ substrate in the presence of analytes.

To address the **second task**, we perform *ab initio* electronic structure and quantum transport calculations of graphene with GBs without the SiO$_2$ substrate, using SIESTA 3.1 and TRANSIESTA [40] DFT-based packages, respectively. We prepared supercells containing pristine graphene regions (electrodes) and defective GBs (sensor) with different local angles with respect to the grains and local defect topologies (Fig. 3). In the transversal direction the cell width is chosen in such a way that a perfect 2D graphene is obtained in the electrode areas and atomic matching is achieved in the GB. Doping of the graphene with GBs by the SiO$_2$ substrate and adsorbed analyte molecules is treated on the model level, using the above obtained results. Despite the fact that graphene grains and GB are differently p-doped in the model system from Fig. 2, the whole systems in Fig.3 are homogeneously p-doped by 0.265e (per unit cell) amount, since the difference in doping is only reflected in slightly different densities of states in the grain contacts. Then, we calculated the electron transmission spectra of such systems. The obtained transmission spectra shift is in a good agreement with the reported experimental doping level (see below). Therefore, to mimic the p-doping form the SiO$_2$ substrate, we calculate the transmission spectrum of each GB by shifting it by ~ 0.15 eV with respect to E$_f$. Further details of the simulations are described in Methods.
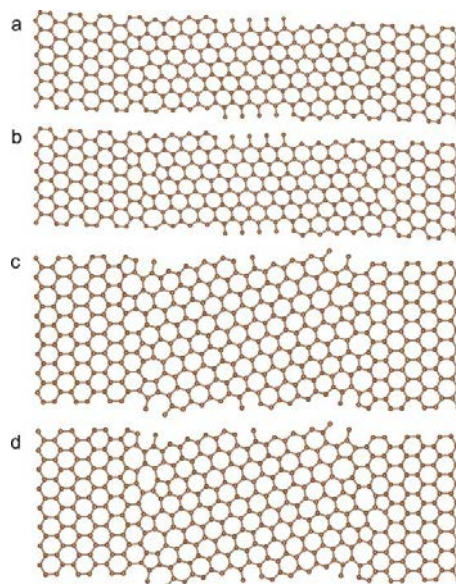

Fig. 3. Supercells for electron transport calculations. (a-b) Unit cells with different defect topologies for nonconductive region (marked by blue in Fig. 6a). (b-d) Unit cells with different defect topologies for conductive region (marked by red in Fig. 6a).

We model the electron transport through the GB system in the presence/absence of adsorbed gas molecules by the Landauer electron transport formula [41] combined with an equilibrium transmissivity obtained in NEGF-based calculations. In this approximation, the electric current density through the GB is given by

$$J = \int Tr(E)\big(n_F(E - \mu_L) - n_F(E - \mu_R)\big)\, dE. \tag{1}$$

Here, *Tr(E)* is the zero bias transmission spectrum of the GB system (Fig. 4) obtained from *ab initio* quantum transport calculations (using TRANSIESTA), $n_F(E - \mu_{L/R})$ are the Fermi-Dirac distribution functions (*T*=300 K) in the left/right grains, respectively, $\mu_{L/R} = E_f \pm V/2$ are the electrochemical potentials in the grains, E_f is the common Fermi energy and *V* is the voltage applied between the grains. The transmission spectra of open channels (solid red line in Fig.4) show sharp onsets of transmission around the transport gap.
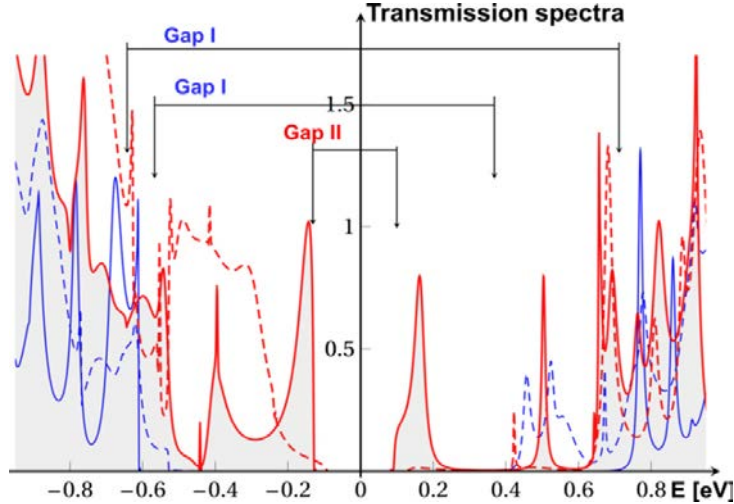

Fig. 4. Transmission spectra of GBs with different translational vectors of left and right grains with different defect topologies. Blue solid and dashed lines show the transmission coefficients for the GBs with supercell units shown in Fig. 3a-b (blue region in Fig. 6a). Red solid and dashed lines show the transmission coefficients for the GBs with supercell units shown in Fig. 3c-d (red region in Fig. 6a). Relative values of the transport gaps are shown.

We calculate the electric currents in the presence and absence of molecules at the GBs using equations 1. In the presence of the DMMP gas molecules adsorbed at the GB, the transmissivity is shifted down. From these currents we calculate the bias-dependent device sensitivity (Fig. 6f),

$$S(V) = \frac{R_{gas}(V) - R_0(V)}{R_0(V)} = \frac{J_0(V) - J_{gas}(V)}{J_{gas}(V) + J_{noise}} , \tag{2}$$

where $J_{noise} \sim 1$ µA is a small noise current. In order to evaluate how the maximal sensitivity depends of the transmission spectra shift ΔE, we use a simplistic transmission model for an ideal conduction channel with an abrupt onset of transmission at $E = E_0$ defined by

$$Tr_0(E) = \begin{cases} 1, & E < E_0 \\ 0, & E \geq E_0 \end{cases} . \tag{3}$$

Then, the electric current is given by the formula:

$$J_0(V) = \int_{-\infty}^{E_0} Tr_0(E)\big(n_f(E - \mu_L) - n_f(E - \mu_R)\big) dE = k_B T \cdot Log\, \frac{1 + e^{\frac{E_0 + eV/2}{k_B T}}}{1 + e^{\frac{E_0 - eV/2}{k_B T}}} , \tag{4}$$

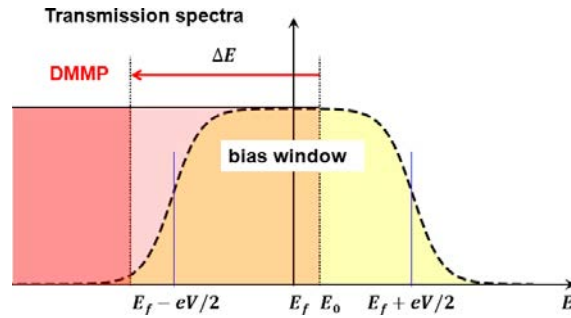where E_f is set to zero and E_0 – is the energy of the transmission onset. Figure 5 illustrates the mechanism.

Fig. 5. Illustration of the model for electron transport calculations. Model transmission spectra for an ideal conduction channel with $Tr_0(E)$ is shown. ΔE – is a shift of the transmission caused by the adsorption of the DMMP gas molecules.

Upon the DMMP gas adsorption, the onset of transmission shifts by ΔE (from its initial energy E_0 to $E_0 - \Delta E$, n-doping effect which is equivalent to the shift of the Fermi energy up by ΔE) resulting in a current of

$$ J_{gas}(V) = k_B T \cdot Log \frac{1 + e^{\frac{E_0 - \Delta E + eV/2}{k_B T}}}{1 + e^{\frac{E_0 - \Delta E - eV/2}{k_B T}}} \ . \tag{5}$$

Be varying the bias (V), one opens or closes the bias widow around the Fermi energy. If the bias widow opens far from the onset of the transmission spectrum (upon the DMMP adsorption) the resulting change of the current will be negligible and sensitivity is small. On the other hand, if the onset of the transmission crosses the bias window in its middle, the further increase of the bias will not lead to the significant change of the current upon adsorption of analytes and the overall sensitivity will be small as well. That explains the non-monotonic behaviour of the sensitivity as a function of the external bias. The peak of sensitivity with respect to bias is reached when the bias window intersects the transmission spectrum of the system after DMMP adsorption. The approximate value of this bias can be calculated using the formula

$$ V_{max} = 2k_B T \cdot \cosh^{-1}\left[\cosh\left(\frac{E_0 - \Delta E + E_f}{k_B T} \right) - 2 \right]. \tag{6}$$

2.3 Computational results

Here, we briefly summarize our results of electronic structure and transport calculations in a typical sensing system. The GB sensing model consists of a quasi-periodic meandered line of defects formed between two graphene grains, with an 18° mismatch angle (consistent with previous TEM studies [21 (1)], deposited on an amorphous SiO_2 substrate, as shown in Fig. 6 a,b. We found that the stress-relaxed structure forms a corrugation along the GB, giving rise to an effective *p - p'- p* doping distribution. The presence of local doping in the GB region is manifested by a calculated two-dimensional (2D) electrostatic potential profile, generated in this area by partial atom charges (Fig. 6c). DMMP molecules with a permanent dipole are attracted to the regions of high electric field gradient present at the *p - p'- p* interface, which results in a local charge donation and modification of the doping distribution (*p – p''- p*). These results are illustrated in Fig. 6d presenting a one-dimensional potential obtained by averaging of the 2D potential along the direction normal to the GB (with and without DMMP molecules).

The meandered GB can be split into local regions (Fig. 6a) with different transport properties, determined by the crystallographic orientation of the graphene grains, the local angle of GB with respect to the grains and the local topologies of GB defects [13,42]. Such regions can be seen to form individual electron transport channels with local transmission spectra (gaps). Depending on the local doping from the substrate (shift of transmission spectra), these transport channels can be initially either opened or closed. Upon adsorption of electron-donating or -accepting analytes

at the GB, the transmission spectra of the channels can be shifted with respect to the Fermi level ($p - p'' - p$). This can open or close some electron transport channels, with a potentially large effect on the GB resistance.
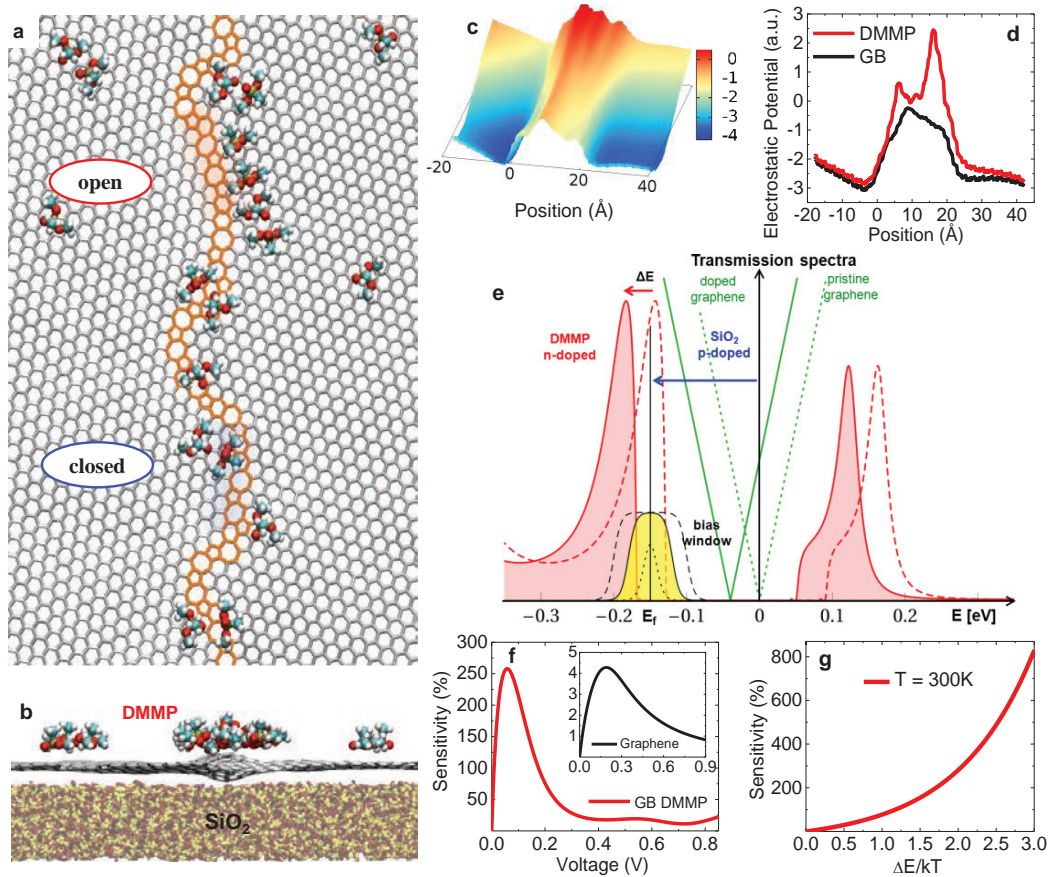

Fig. 6 Classical and quantum simulation studies. (a) The top and (b) side views of the modelled graphene grain boundary structure deposited on the defective amorphous SiO$_2$ substrate with physisorbed DMMP molecules. Two transmission regions with different translational vectors are highlighted in red (small gap) and blue (large gap) colors. (c) Two-dimensional electrostatic potential energy profile across the GB. (d) One-dimensional potential profiles (with and without DMMP molecules) obtained by averaging of the 2D potential along the direction normal to the GB. (e) Calculated transmission spectra (red curves) for the open GB region (highlighted in red in Fig. 6a) and the grain region (green dashed line), shown both without and with homogeneous n-doping (green solid line) by DMMP molecules (same adsorbents surface density). The Fermi level, E$_f$, is shifted down (Dirac point of the grains) due to the p-doping by SiO$_2$. Bias window intersects spectra of certain transmission regions and opens the passage of electrons through them, while adsorbed DMMP molecules tend to close these passage regions. (f) Calculated sensitivity for the GB and graphene grain (inset) with respect to the applied voltage for DMMP molecules. (g) Maximum sensitivity calculated as a function of a DMMP-induced spectral shift over a thermal energy, $\Delta E / kT$.

To illustrate these phenomena, we have calculated the local electron transmission through two selected GB regions (shown in Fig. 6a) with different local angles and defect topologies (Figs 2 and 3). Once these local regions are arranged in a periodic manner (Fig.3), their zero-bias transmissivity is shown in Fig.4. One can see that the transport of electrons with energies close to E$_f$ is strongly suppressed through these systems made of local regions. The transmittance reveals different transport gaps (~0.2 eV, ~ 1 eV) for the two GB regions. We assume that only regions with the smallest energy gaps and energy onsets can significantly contribute to the molecular sensing. Note that

graphene GBs feature isolated states near E_f [13,38,42-47]. However, these spatially localized states are not visible in the GB transmissivity, since they do not overlap with the electrode states.

Figure 6e shows the equilibrium transmission spectrum through the low-gap (0.2 eV) region before (red-dashed curve) and after (red-shadowed curve) adsorption of DMMP molecules (detail of Fig. 4). Since the graphene subsystem is p-doped by SiO_2, E_f (thin black line) in Fig. 6e is shifted downwards (by ~ 0.15 eV) from the zero-level energy (non-doped case). In the presence of DMMP, GB is additionally n-doped, as shown by a shifted transmission spectrum down (by ~ 0.05 eV) with respect to E_f, assuming that E_f stays fixed with respect to the rest of the system (grains transmission spectra shown by green dashed lines). The 0.05 eV shift corresponds to an electron density concentration of ~ 2.5×10^{11} cm^{-2}, which is compatible with DMMP/graphene experimental values [39]. We used these two spectra to calculate from equations 1-6 an electron current passing through the GB region under bias (yellow area in Fig. 6e) in the presence and absence of homogenously distributed DMMP molecules. One can see that for the p-doped system the current flow passes (windows overlap with GB spectrum), while when DMMP n-dopes GB, the current does not flow (no overlap) unless bias is increased enough (Fig. 5).

Finally, Fig. 6f presents the obtained bias-dependent sensitivities (Eqns. 1 and 2) for DMMP analytes for both GB (channel region) and pristine graphene (inset figure) under the same doping conditions (substrate and density of DMMP), showing a prominent sensitivity peak, in agreement with our experiments [14]. The used transmission spectra are shown by red and green lines in Fig. 6e (pristine graphene needs more exposure to the adsorbants for the same DMMP surface density). Because of the sharp transmission onset of the GB transport channel (Fig. 6e), the calculated maximum sensitivity (250%) is 60 times larger than that of graphene (4%). Using a simplified analytical model (Eqn. 3), we have performed additional calculations to find out how the maximum sensitivity of the GB device depends on the transmission spectra shift, ΔE, caused by the local adsorption of analytes (Fig. 6g). We found that an n-doping shift of $0.08 eV \approx 3 k_B T$ is required to achieve the ~ 800% experimentally observed sensitivity. This shift of the GB spectrum seems to be realistic due to the additional accumulation of the DMMP molecules adsorbed around the GB (Fig. 6d). The presented sensing mechanism has an inherent symmetry for electron-donating and electron-accepting analytes. To obtain maximum sensitivity for each case, the Fermi level should be tuned by gate doping closely below (above) the energy onset for the electron donors (acceptors), hence they can close (open) the electron transport channels.

3. Carbon dioxide reduction on molybdenum disulphide edges

3.1 *Experimental evidence of the superior catalytic activity of Mo-terminated MoS₂ edges*

Recently [20], one of the highest CO_2 reduction performance was demonstrated in layer-stacked bulk MoS_2 with Mo-terminated edges solvated in 1-ethyl-3-methylimidazolium tetrafluoroborate (EMIM-BF$_4$) ionic liquid (4 mol% EMIM-BF$_4$) and 96 mol% water. EMIM-BF$_4$ was deliberately selected due to its particular catalytic features, which made the system more selective for carbon monoxide (CO) formation than hydrogen (H_2) production [19,48,49]. Figure 7a represents the CV curve for the CO_2 reduction in this system. The CO_2 reduction equilibrium potential is -0.11V versus reversible hydrogen electrode (RHE) in the protic media [19,26]. The reduction reaction initiates at -0.164V, as confirmed by measuring CO as a product by gas chromatography (GC) system (CO Faradaic efficiency FE ~ 3%). This results in a very low overpotential (54 mV) for CO formation in our system. Moreover, MoS_2 demonstrates far more exceeding catalytic characteristics than those of commonly used Ag nanoparticles. The high catalytic activity of bulk MoS_2 was attributed to the Mo-terminated edges and further experimentally supported by the carbon dioxide reduction performance of vertically aligned MoS_2.
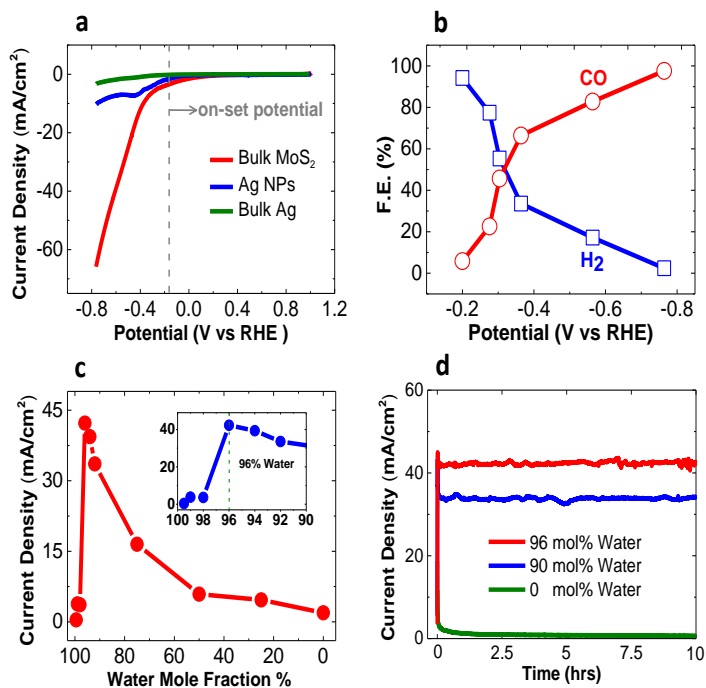
Fig. 7 CO_2 reduction performance of the bulk MoS_2 catalyst in the EMIM-BF$_4$ solution. (a) Cyclic voltammetric (CV) curves for bulk MoS_2, Ag nanoparticles (Ag NPs) and bulk Ag in CO_2 environment. The experiments were performed in 96mol% water and 4mol% EMIM-BF$_4$ solution by sweeping applied potential from +1V to -0.764V versus RHE. The vertical grey line indicates the low overpotential (~54mV) for CO_2 reduction at bulk MoS_2. (b) CO and H_2 Faradaic efficiency (FE) at different applied potentials. (c) The current density of CO_2 reduction (measured by Chrono-Amperometry) at 0.764V versus RHE as a function of water mole fraction in EMIM-BF4 electrolyte. The maximum current density was recorded in 96mol% water - 4mol% EMIM-BF$_4$ electrolyte (inset). (d) Chrono-Amperometry results of MoS2 catalyst in different solutions (96, 90 and 0mol% water) showing negligible loss in current density even after 10 h. [20]

3.2 *Simulations of catalytic performance of Mo-terminated edges of MoS$_2$*

To disclose the origin of the high catalytic activity of MoS_2 edges, we have used hybrid modeling techniques addressing different aspects of the experimental systems. We have performed (1) spin-polarized DFT calculations of the electronic structure of MoS_2 flakes and (2) quantum molecular dynamics (QMMD) simulations of EMIM ions interacting with CO_2 molecules in condensed phase.

To address the **first task**, we have used DFT methods to calculate the projected density of states (PDOS) per different Mo and S atoms [50-52] for MoS_2 flakes. As suggested by STEM measurements, the bulk Mo atoms, sandwiched between two S layers, are not directly exposed to the electrolyte, so the MoS_2 catalytic activity should be primarily related to the edge states formed by Mo-edge atoms. Therefore, we have modeled MoS_2 ribbons (single- or double layered) with properly arranged edge terminated atoms (see Fig. 8). Next we analyzed the contributions of edge versus bulk atoms to the total density of electronic states (DOS) of MoS_2 flakes. We used SIESTA 3.1 [40] with the Perdew-Burke-Ernzerh exchange-correlation functional [53] and the norm-conserving Troullier-Martins pseudopotentials [54] to describe valence electrons. The calculations were performed on a real-space grid with a mesh cutoff of 400 Ry within the eigenvalue tolerance of 10^{-4} eV, using a DZP (double-zeta basis and polarization orbitals) basis set. The Brillouin zones of the unit cells were sampled by the Monkhorst-Pack grid with a spacing between k-points of $\Delta k < 0.01 Å^{-1}$. The geometry optimization was carried out within the conjugated gradient algorithm, until all the forces are F<0.04 eV per Å and the stress in the periodic direction is $\sigma < 0.01$ GPa.
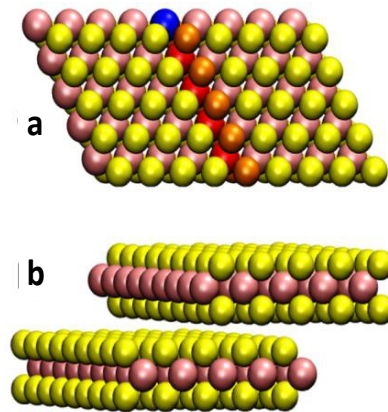
Fig. 8 MoS_2-nanoribbon structure. (a) A single layer nanoribbon. Mo-atoms are pink, S-atoms are yellow. In the unit cell bulk Mo-atoms are red, edge Mo-atom is blue, and S-atoms are orange. (b) Shifted double layer (side view).

To address the **second task**, we have performed quantum molecular dynamics simulations (TeraChem) [37] of the $[EMIM-CO_2]^+$ complex hydrated in quantum water. The energies and forces were evaluated using the B3LYP exchange-correlation functional with 3-21 g basis set with DFT-D3 dispersion corrections [37,55]. The charges were calculated within the Mulliken scheme. We have tested the effect of different pH of the solution on the $[EMIM-CO_2]^+$ complex stability in several possible configurations. We have described quantum mechanically one $EMIM^+$ ion, one CO_2 molecule and 99 water molecules, surrounding $EMIM^+$ and CO_2. The remaining (2,500) waters were described classically with the TIP3P force-field. We have added in the quantum water either one Cl^- counter ion, in order to make the whole system neutral. We have added there also one H_3O^+ ion and one more Cl^- counter ion (neutrality), in order to properly model the current experiments, performed at pH=4. In this way, we roughly got H_3O^+ ion per 100 quantum water molecules (2,600 in total).
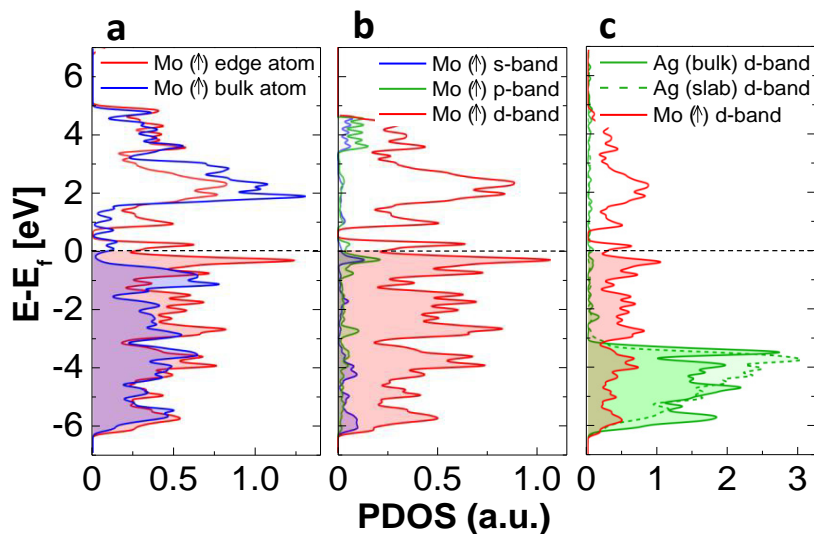

Fig. 9 DFT calculations of electron density. PDOSs for spin-up channel of: (a) the Mo atom at the edge and Mo atom within the lattice; (b) s, p, and d-orbital of Mo-edge atom. (c) PDOS of d band of Mo-edge atom, Ag atom from bulk and Ag-slab of 8.32-Å thickness. Electron density on Mo-edge atom is significantly (~11 times) higher than the electron density on Ag atom.

3.3 *Computational results*

The density of states at the Fermi energy level (E_f) roughly determines the availability of electrons for a given reaction [51]. We found that the electronic structure of MoS_2 ribbons near E_f is formed by edge bands of only one-spin polarization, originating from the Mo and S atoms exposed at both MoS_2 edges. In the vicinity of E_f, the spin-polarized PDOS for these Mo atoms is approximately twice larger than that of the bulk Mo atoms (Fig. 9a). Next, we resolved the PDOS of the Mo-edge atoms into s-, p and d-orbital electron contributions (Fig. 9b). The obtained data indicate that near E_f, the PDOS is dominated by d-orbital (Mo) electron states, which are known to actively participate in catalyzed reactions [51]. The S atoms possess less reactive p orbitals and they are not present at the catalytically active edge sites (confirmed by STEM) [14].
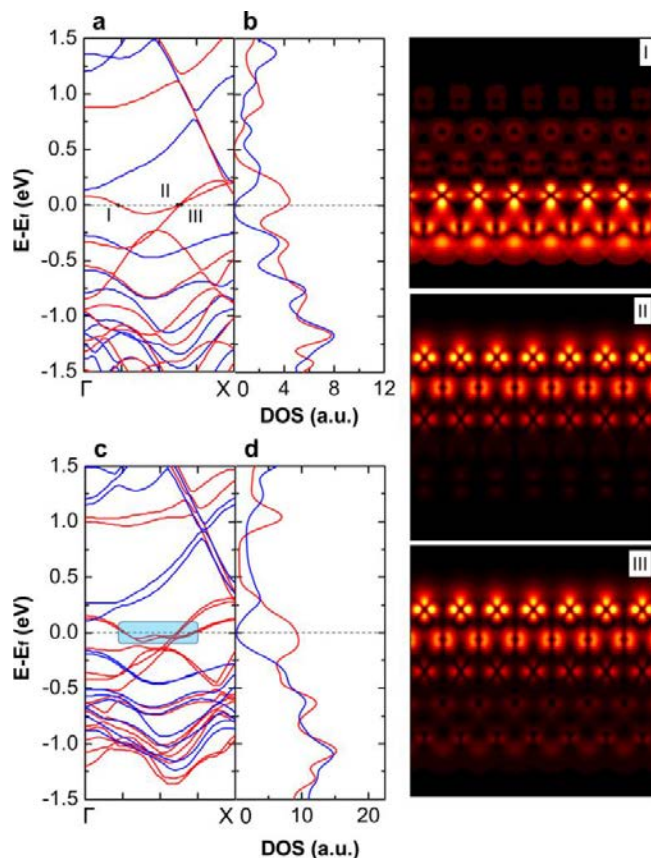

Fig. 10 Electronic structure of single and shifted double layer MoS_2-nanoribbon. (a) and (c) show band structures of MoS_2 single and double layer, respectively. (b) and (d) show the total DOS for corresponding structures. The red and blue lines denote the α- and β-spin channel bands, respectively. I, II, and III illustrate spatial profiles of modulus of wavefunctions for corresponding metallicity points (Mo-edge is at the top, S-edge is at the bottom).

From the spin-resolved electronic structure of the single and double layer MoS_2-nanoribbons (Fig. 10 a-d), one can see that only spin-up bands cross the Fermi energy. We analyzed the character of the (I, II, III) metallicity points in the single layer MoS_2 by visualizing the corresponding wavefunctions forming one dimensional metallic edge states. The wavefunctions at the first metallic point I is localized at the S-edge of the strip, whereas the wavefunctions at the points II and III are localized at the Mo-edge, as observed in previous studies [56,57]. In the presence of two layers, the bands associated with edge states split and become flatter, as highlighted in Fig. 10c. After normalization per

number of atoms in the unit cell (division of red DOS in Fig. 10b by 15 and in Fig. 10 d by 30), DOS for the double layer gave a slight increase due to the flattering of the bands near the Fermi energy (highlighted by a blue square in Fig. 10c). This DOS accumulation contributes to the high catalytic rates observed in the experiments. Additional layers in the bulk MoS_2 substrate could further enhance the DOS. The Mo d-electrons form metallic edge states [56], which can freely supply electrons to the reactants attached at the edges. To assess how the Mo-edge states are affected by the presence of additional MoS_2 layers, we performed the same analysis for a double-layer MoS_2 strip. Our calculations showed that an interlayer coupling further increases the d-electron PDOS near E_f (Fig. 10a-d). In the presence of an external bias, all these d-electron states near E_f can be accessed in the reaction, supporting the large observed MoS_2 activity.

We have also compared the d-orbital PDOS in Mo-edge atoms with that in Ag atoms in two structures: a bulk Ag and a two-dimensional slab Ag (both fcc lattice with a lattice constant of 4.09 Å) of a 8.32-Å thickness (after relaxation) (Fig. 9c). We found that the d-band center for Mo-edge atoms is closer to the Fermi energy level than that in both Ag structures. This can partly explain the high catalytic activity of MoS_2, since the higher the d-band center is, the more reactive the metal is due to a lower transition state energy [51]. Moreover, the PDOS of Mo-edge atoms near E_f is approximately one order of magnitude higher than the PDOS of Ag atoms, suggesting the availability of the excess of d electrons on the Mo-edge atoms. We believe that both these factors are responsible for the high CO_2 reduction current density of MoS_2.
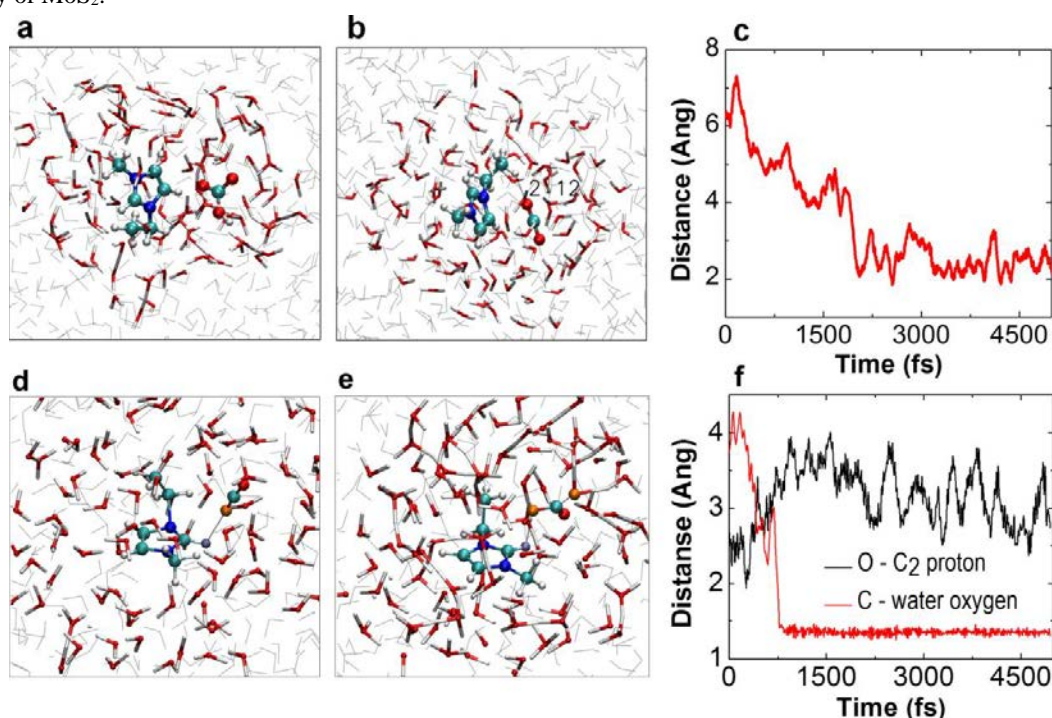

Fig. 11 Formation and stability of $[EMIM-CO2]^+$ complex. First row (complex near the C4 proton): (a) Formation of the $[EMIM-HCO_3]$ complex in neutral conditions. (b) Formation of the $[EMIM-CO_2]$ complex in acidic conditions. (c) Time dependence of the hydrogen bond length formed between CO_2 and $EMIM^+$. Second row (complex near the C2 proton in acidic pH): (d) Initial configuration $[EMIM-CO_2]$ complex with the H-bonds shown between the C2 proton (highlighted byce ice blue) and the oxygen (highlighted by orange) from CO_2. (e) Stabilization of the $[EMIM-CO_2]$ complex with an additional coordination of CO_2 and a water molecule (the oxygen is highlighted by orange). (f) Time dependence of the hydrogen bond length between CO_2 and $EMIM^+$ and between CO_2 and an adjacent water molecule.

Finally, we have modelled the CO_2 delivery towards MoS_2 surface to see the role of EMIM ions. It is well known [58] that the solvation of CO_2 in water results in the formation of various species among which HCO_3^- and CO_3^{2-} are

the dominant in neutral and basic conditions, respectively. Our simulations revealed that the $EMIM^+$ cation can form different complexes with CO_2 stabilized by hydrogen bonding (Fig. 11), where CO_2 may be coordinated to $EMIM^+$ ion by hydrogen bond either through the most acidic proton C2 [59,60] or less acidic protons C4/C5 (compare Fig. 11 b and d). However, the complex (CO_2) stability depends on the pH of the electrolyte, temperature and concentration of IL.

Using QM/MM simulations, we found that when CO_2 is initially positioned around C4/C5 protons in neutral solution, the $[EMIM-CO_2]^+$ complex forms, but it reacts within ~2 ps with water molecules and forms either the $[EMIM-HCO_3]$ or $[EMIM-CO_3]^-$ complexes (Fig. 11a). In acidic environment, similar to our experimental conditions (pH<4), the simulations show that the $[EMIM-CO_2]^+$ complex remains stable (t~10 ps) (Fig. 11b) and CO_2 stays in the linear configuration. The average length of the H-bond between the C4 proton and O-atom of CO_2 is ~ 2.4 Å (Fig. 11c). However, the QM/MM simulations of $EMIM^+$ ion and CO_2 positioned around the C2 proton (Fig. 11d) revealed that the $[EMIM-HCO_3]$ complex tends to form even in acidic environment (Fig. 11e). The origin of this process is a higher polarizability of the C2-H bond (compared to e.g. the C4-H bond). The average length of the H-bond between the C2 proton and the O atom of CO_2 is relatively long, ~ 3.2 Å (Fig. 11f). Therefore, this binding configuration might be less stable than the C4/5-H binding configuration. Moreover, since the reduction of the $[EMIM-HCO_3]$ complex in the aqueous phase would lead to the production of a formic acid, which is not observed in our experiments, we conclude that the $[EMIM-CO_2]$ complex most likely forms at the C4 site.

These results agree with previous in situ $[EMIM-CO_2]$ complex formation studies [48]. The $[EMIM-CO_2]^+$ complexes could potentially physisorb (Coulombic and van der Waals coupling) [19,48,49] at the (negatively charged) MoS_2 cathode, resulting in a close encounter of the CO_2 molecules with the MoS_2 surface. The presence of $EMIM^+$ cations around CO_2 molecules can reduce the reaction barrier for electrons passing into CO_2. Thus, the observed high-CO_2 reduction reaction is attributed to a synergistic action of the MoS_2 catalyst and the $EMIM-BF_4$ ionic liquid. While $EMIM-BF_4$ has a crucial role by reducing the overpotential for the reaction, the CO_2 reduction rate is mainly governed by the intrinsic properties of the MoS_2 catalyst. Ultraviolet photoelectron spectroscopy also indicated that the work function of MoS_2 (3.9 eV) is significantly lower than that of the bulk Ag (4.37 eV) and Ag NPs (4.38 eV) [58]. Due to the low work function of MoS_2, the abundant metallic-like d-electrons in its edge states can take part in the reactions, ultimately resulting in the superior CO_2 reduction performance compared with Ag.

4. Conclusions

In summary, we have used hybrid computational methods to investigate the electronic and catalytic properties of low-dimensional structural features in graphene (graphene grain boundaries) and molybdenum disulphide (localized 1D metallic edge states). A combination of quantum and classical structural and transport approaches have allowed decipher the complexity behind the unique experimental observations in these nanosystems. It was shown that the sensitivity of an isolated GB is ~300 times higher than that of a single graphene grain and much larger than that of polycrystalline graphene sensors. We have verified that the presence of local transport gaps in GBs together with the local accumulation of gas molecules plays a crucial role in the observed large chemical sensitivity of GBs, so the mechanism differs from the previously reported carrier density modulation in carbon-based sensors. The sensing mechanism is based on a marked closing or opening of local conduction channels through the GB by the adsorbed analytes. This new sensing modality can be used to develop real nanometre-scale sensors with numerous potential applications. We also have shown that the highest observed catalytic performance of MoS_2 for the CO_2 reduction (relative to noble metal catalysts) is mainly attributed to a high density of d electrons in Mo-terminated edges and also to its low work function. Based on our findings, MoS_2 –flakes can be suggested as effective replacement of expensive noble metal electrodes, with the promise of higher CO_2 conversion rates and selectivity. These studies illustrate how to model future nanoscale material systems with highly complex structures and behaviors.

5. Methods

5.1 Molecular sensing

The classical MD simulations are performed using the Langevin dynamics with a damping constant of $\gamma_{Lang} = 1$ ps^{-1}. The systems are simulated in an NVT ensemble at a temperature of T=300 K, where the particle mesh Ewald summation [34] is used to describe long-range Coulomb coupling; the switching distance for non-bonded interactions

is set to 8 Å, and the cutoff is set to 10 Å. In the quantum MD simulations, the classical force field is corrected in a stepwise manner to obtain partial charges of atoms, which are necessary to describe local adsorption of molecules at the GB. The quantum simulations are performed with TeraChem [35-37] package, where energies and forces are evaluated using the Becke, Lee, Yang and Parr (BLYP) exchange-correlation functional with a 3-21-g basis set. To account more accurately the effects of non-covalent bonding, the charge transfer between graphene grains/GBs, amorphous SiO_2 and DMMP molecules is obtained within the Mulliken scheme by the BLYP functional with dispersion corrections (the revised DFT-D3 method) [37].

In the electron transport calculations, we used the Perdew-Burke-Ernzerh of exchange-correlation functional [53] and the norm-conserving Troullier-Martins pseudopotentials [54] to describe valence electrons. The calculations were performed on a real-space grid with a mesh cut-off of 400 Ry within the eigenvalue tolerance of 10^{-4} eV, using a SZP (single-zeta basis and polarization orbitals) basis set. In the used supercells, shown in Fig. 3, the distances between neighboring GBs are chosen to be ~2.5-3 nm in order to exclude their mutual elastic interactions. The geometry optimization was carried out within the conjugated gradient algorithm, until all the forces are F < 0.04 eV/Å and the stress in the periodic direction is σ < 0.01 GPa. The Brillouin zones of the unit supercells were sampled by the Monkhorst-Pack grid with 3-5 *k*-points along the direction parallel to the GBs and 5 *k*-points along the electron transport direction. The convergence of the transmission spectra with respect to the *k*-points sampling was achieved.

5. Acknowledgements

6. References

[1] K. S. Novoselov et al. Science 306 (2004) 666.

[2] A.H. Castro Neto et al. Rev. Mod. Phys. 81 (2009) 109-162

[3] F. Cervantes-Sodi, G. Csanyi, S., Piscanec, and A.C. Ferrari, Phys. Rev. B 77, (2008) 165427.

[4] J.A. Furst et al. New J. of Phys. 11 (2009) 095020.

[5] A. Baskin, P. Kral, Sci. Reports 1 (2001) 36.

[6] P.G. Collins, Science 287 (2000) 1801-1804.

[7] J. A. Robinson, E.S. Snow, S.C. Badescu, T.L. Reinecke, and F.K. Perkins, Nano Lett. 6, (2006) 1747-1751.

[8] J.T. Robinson, F.K. Perkins, E.S. Snow, Z. Wei and P.E. Sheehan, Nano Lett. 8 (2008) 3137-3140.

[9] T.O. Wehling, et al. Nano Lett. 8 (2008) 173-177.

[10] J.D. Fowler et al. ACS Nano 3 (2009) 303-306.

[11] Y.-H. Zhang et al. Nanotechnology 20 (2009) 185504.

[12] A. Salehi-Khojin et al. Appl. Phys. Lett. 100 (2012) 033111.

[13] O.V. Yazyev, and S.G. Louie, Nat. Mater. 9 (2010) 808-809.

[14] P. Yasaei et al. Nat. Commun. 5 (2014) 4911.

[15] T.F. Jaramillo et al. Science 317 (2007) 100-102.

[16] T. Wang et al. Chem. Eur. J. 19 (2013) 11939-11948.

[17] H.I. Karunadasa et al. Science 335 (2012) 698-702.

[18] B. Hinnemann et al. J. Am. Chem. Soc. 127 (2005) 5308-5309.

[19] B.A. Rosen et al. Science 334 (2011) 643-644.

[20] D.T. Whipple and P.J.A. Kenis, J. Phys. Chem. Lett. 1 (2010) 3451-3458.

[21] B. Kumar et al. Nat. Commun. 4 (2013) 2819.

[22] B.A. Rosen et al. Science 334 (2011) 643-644.

[23] B.A. Rosen et al. J. Phys. Chem. C 116 (2012) 15307-15312.

[24] A. Salehi-Khojin et al. J. Phys. Chem. C 117 (2013) 1627-1632.

[25] Y. Chen, C.W. Li and M.W. Kanan, J. Am. Chem. Soc. 134 (2012) 19969-19972.

[26] C.W. Li and M.W. Kanan, J. Am. Chem. Soc. 134 (2012) 7231-7234.

[27] N. Hoshi, J. Electroanal. Chem. 440 (1997) 283-286.

[28] B.A. Rosen, W. Zhu, G. Kaul, A. Salehi-Khojin and R.I. Masel, J. Electrochem. Soc. 160 (2013) H138-H14.

[29] Q. Lu et al. Nat. Commun. 5 (2014) 3242.

[30] M. Asadi et al. Nat. Commun. 5 (2014) 4470.

[31] F. Schedin et al. Nat. Mater. 6 (2007) 652-655.

[32] J.C. Phillips et al. J. Comput. Chem. 26 (2005) 1781-1802.

[33] W. Humphrey, A. Dalke, and K. Schulten, J. Mol. Graph. 14, (1996) 33-38, 27-28.

[34] A.D. MacKerell et al. J. Phys. Chem. B 102 (1998) 3586-3616.

[35] J. Kastner et al. J. Phys. Chem. A 113 (2009)11856-11865.

[36] I.S. Ufimtsev and T. J. Martinez, J. Chem. Theory Comput. 5(2009) 2619-2628.

[37] S. Grimme, J. Antony, S. Ehrlich and H.A. Krieg, J. Chem. Phys. 132 (2010) 154104.

[38] J.C. Koepke et al. ACS Nano 7 (2013) 75-86.

[39] B. Kumar et al. Nano Lett. 13 (2013) 1962-1968.

[40] D. Sanchez-Portal, P. Ordejon, E. Artacho and J.M. Soler,. Int. J. Quantum Chem. 65 (1997) 453–461.

[41] P. Král, F. Sheard, and F. Ouali, Phys. Rev. B 57 (1998) 15428–15438.

[42] J. Zhang, J. Gao, L. Liu and J. Zhao, J. Appl. Phys. 112 (2012) 053713.

[43] K. W. Clark et al. ACS Nano 7 (2013) 7956-7966 .

[44] L. Tapaszto et al. Appl. Phys. Lett. 100 (2012) 053114.

[45] J. Cervenka, M.I. Katsnelson and C.F. J. Flipse, Nat. Phys. 5 (2009) 840-844.

[46] J. Cervenka and C. Flipse, Phys. Rev. B 79 (2009) 195429.

[47] O.V. Yazyev and S.G. Louie, Phys. Rev. B 81 (2010) 195420.

[48] B.A. Rosen et al. J. Phys. Chem. C 116 (2012) 15307-15312.

[49] A. Salehi-Khojin et al. J. Phys. Chem. C 117 (2013) 1627-1632.

[50] C.G. Vayenas, S. Bebelis and S. Ladas, Nature 343 (2008) 625-627.

[51] B. Hammer and J.K. Norskov, Adv. Catal. 45 (2000) 71-129.

[52] A.R. Botello-Mendez, F. Lopez-Urias, M. Terrones and H. Terrones, Nanotechnology 20 (2009) 325703-325706.

[53] J. Perdew, K. Burke, and Y. Wang, Phys. Rev. B 54 (1996) 16533–16539.

[54] N. Troullier and J. Martins, Phys. Rev. B 43 (1991) 8861–8869.

[55] S. Grimme, S. Ehrlich, and L. Goerigk, J. Comput. Chem. 32 (2011) 1456-1465.

[56] Y. Li, Z. Zhou, S. Zhang and Z. Chen, J. Am. Chem. Soc. 130 (2008) 16739-16744.

[57] R.R. Chianelli et al. Catal. Rev. 48 (2006) 1-41.

[58] A.H. England et al. Chem. Phys. Lett. 514 (2011) 187-195.

[59] T.C. Lourenco, M.F. Coelho, T.C. Ramalho, D. Spoel and L.T. Costa, Environ. Sci. Technol., 47 (2013) 7421-7429.

[60] J.S. Wilkes and M.J. Zaworotko, J. Chem. Soc., Chem. Commun. 15 (1992) 965-967.